Appl. Math. Mech. -Engl. Ed., **40**(7), 1001–1016 (2019)

Applied Mathematics and Mechanics (English Edition)

https://doi.org/10.1007/s10483-019-2498-8

Postbuckling analysis of functionally graded graphene platelet-reinforced polymer composite cylindrical shells using an analytical solution approach*

S. BLOORIYAN[1], R. ANSARI[1], A. DARVIZEH[1], R. GHOLAMI[2,†], H. ROUHI[3]

1. Department of Mechanical Engineering, University of Guilan, Rasht 41635-3756, Iran;
2. Department of Mechanical Engineering, Lahijan Branch, Islamic Azad University, Lahijan 44169-39515, Iran;
3. Department of Engineering Science, Faculty of Technology and Engineering, University of Guilan, Rudsar-Vajargah 44891-63157, Iran

(Received Aug. 10, 2018 / Revised Jan. 12, 2019)

Abstract An analytical approach is proposed to study the postbuckling of circular cylindrical shells subject to axial compression and lateral pressure made of functionally graded graphene platelet-reinforced polymer composite (FG-GPL-RPC). The governing equations are obtained in the context of the classical Donnell shell theory by the von Kármán nonlinear relations. Then, based on the Ritz energy method, an analytical solution approach is used to trace the nonlinear postbuckling path of the shell. The effects of several parameters such as the weight fraction of the graphene platelet (GPL), the geometrical properties, and distribution patterns of the GPL on the postbuckling characteristics of the FG-GPL-RPC shell are analyzed.

Key words cylindrical shell, nanocomposite, graphene platelet (GPL), postbuckling, analytical solution

Chinese Library Classification O343
2010 Mathematics Subject Classification 82D60, 82D80, 74K25, 82B21, 74G10, 74G60

1 Introduction

Shell-type structures as load-carrying components have many applications in mechanical, architectural, civil, marine, and aeronautical engineering fields. Therefore, studying their mechanical behaviors (vibration and buckling) is of great importance. In particular, the buckling problem of shells and plates has been the subject of research works by numerous scientists and engineers. In the following, some of the recent papers in this field are cited.

* Citation: BLOORIYAN, S., ANSARI, R., DARVIZEH, A., GHOLAMI, R., and ROUHI, H. Postbuckling analysis of functionally graded graphene platelet-reinforced polymer composite cylindrical shells using an analytical solution approach. *Applied Mathematics and Mechanics* (*English Edition*), **40**(7), 1001–1016 (2019) https://doi.org/10.1007/s10483-019-2498-8

† Corresponding author, E-mail: gholami_r@liau.ac.ir

©Shanghai University and Springer-Verlag GmbH Germany, part of Springer Nature 2019

Zhu et al.[1] analyzed the buckling of unstiffened cylindrical shells subject to external pressure by experimental tests and the finite element method (FEM). Within the framework of Reddy's shear deformation shell theory and using von Kármán's assumptions, Li et al.[2] addressed the postbuckling problem of anisotropic laminated cylindrical shells under combined axial compression and external pressure. Also, the buckling and postbuckling characteristics of aforementioned shells in the thermal environment were studied by Li and Qiao[3] using a singular perturbation method. The buckling and postbuckling behaviors of heated cylindrical shells made of functionally graded materials (FGMs) exposed to combined compressive axial loading and radial pressure were analyzed by Huang and Han[4] with an analytical approach. Based on the Donnell shell theory and using the Ritz energy method, Shakouri et al.[5] studied the torsional buckling of simply-supported laminated conical shells. Sofiyev[6] presented a numerical analysis on the buckling of sandwich conical shells made of FGMs subject to hydrostatic pressure based on the first-order shear deformation shell theory. Based on the modified couple stress theory, a three-dimensional solution was provided by Guo et al.[7] for anisotropic multilayered composite plates. Also, Guo et al.[8] used the two-dimensional Fourier series to examine the size-dependent behavior of functionally graded (FG) anisotropic composite plates.

In recent years, the reinforcement of composites with nanomaterials has attracted a lot of attention from the researchers. Especially, the excellent mechanical properties of carbon nanotubes (CNTs)[9] have made them ideal candidates for the reinforcement of composite materials. Carbon nanotube-reinforced composites (CNTRCs) are advanced materials with numerous potential applications[10–15]. One can find numerous research works in the literature in which synthesizing CNTRCs has been reported[16–21]. Also, graphene and its derivatives are used for the reinforcement of polymer composites. High strength and stiffness, low production cost, low density and abundance in nature can be mentioned as the advantages of using the graphene in the aforementioned nanocomposites[22–23].

Graphene platelet-reinforced polymer composites (GPL-RPCs) belong to a new class of functional materials with unique properties which make them excellent candidates for several applications[24]. There are some investigations into the mechanical analysis of structural elements made of GPL-RPCs[25–30]. For example, Gholami and Ansari[31] proposed a numerical approach to study the nonlinear bending of multilayer FG-GPL-RPC rectangular plates under uniform and sinusoidal transverse loads. Wang et al.[32] addressed the buckling problem of graphene platelet-reinforced composite (GPL-RC) cylindrical shells with the cutout. They also investigated the eigenvalue buckling of FG-GPL-RC cylindrical shells with the FEM[33]. The buckling and postbuckling responses of FG-GPL-RC beams embedded in an elastic foundation were analyzed by Yang et al.[34].

In the current work, a Ritz-based analytical approach is used to address the nonlinear buckling and postbuckling problems of FG-GPL-RPC cylindrical shells subject to combined compressive axial and lateral pressure loads. The Halpin-Tsai model and the rule of mixture are used to calculate the material properties of the nanocomposite. The geometrically nonlinear governing equations are also derived based on the classical Donnell shell theory and the von Kármán-type geometric nonlinearity. Selected numerical results are presented to study the effects of graphene platelet (GPL) nanofillers and geometrical properties on the nonlinear buckling and postbuckling characteristics of the FG-GPL-RPC shell.

2 Material properties

Figure 1 shows a cylindrical shell made of the FG-GPL-RPC. As indicated, four patterns are considered for the distributions of the GPL across the thickness direction of the shell.

It is assumed that the weight fraction of the GPL changes across the thickness in a layer-wise manner. For each distribution pattern, the volume fraction of GPL of the kth layer is given by

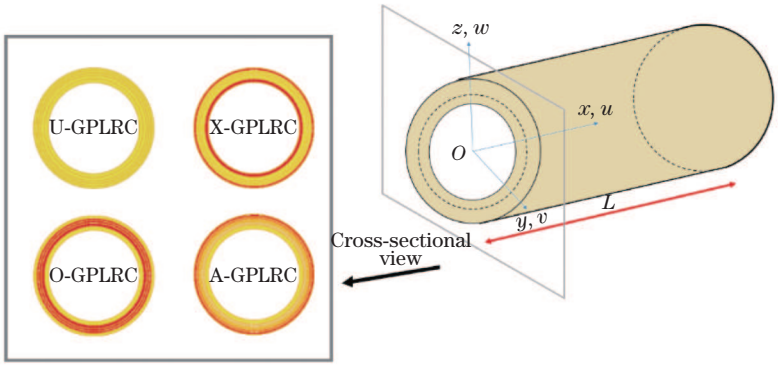

Fig. 1 FG-GPL-RPC cylindrical shell with different patterns of GPL distributions

$$\text{U-GPLRC}: V_{\text{GPL}}^{(k)} = V_{\text{GPL}}^{*}, \tag{1a}$$

$$\text{X-GPLRC}: V_{\text{GPL}}^{(k)} = 2V_{\text{GPL}}^{*}\left|2k - N_{\text{L}} - 1\right|/N_{\text{L}}, \tag{1b}$$

$$\text{O-GPLRC}: V_{\text{GPL}}^{(k)} = 2V_{\text{GPL}}^{*}\Big(1 - \frac{\left|2k - N_{\text{L}} - 1\right|}{N_{\text{L}}}\Big), \tag{1c}$$

$$\text{A-GPLRC}: V_{\text{GPL}}^{(k)} = V_{\text{GPL}}^{*}\left(2k - 1\right)/N_{\text{L}}, \tag{1d}$$

where $k = 1, 2, \cdots, N_{\text{L}}$, and

$$V_{\text{GPL}}^{*} = \frac{w_{\text{GPL}}}{w_{\text{GPL}} + (1 - w_{\text{GPL}})\Big(\dfrac{\rho_{\text{GPL}}}{\rho_{\text{m}}}\Big)}, \tag{2}$$

in which ρ_{GPL} and ρ_{m} are used to show the mass densities of the GPL and matrix, respectively.

One can use the modified Halpin-Tsai model to calculate the material properties of GPL-RPCs with a low content of GPLs. For GPL-RPCs with the low content of GPLs, the accuracy of this model is validated by the experiments performed by Rafiee et al.[35]. Based on the model, the effective elastic modulus is approximated as

$$E_{\text{eff}} = \frac{3}{8}E_{\text{L}} + \frac{5}{8}E_{\text{T}}, \tag{3}$$

where E_{L} and E_{T} denote the longitudinal and transverse elastic moduli, respectively. They are formulated as

$$E_{\text{L}} = \frac{1 + \xi_{\text{L}}\eta_{\text{L}}V_{\text{GPL}}}{1 - \eta_{\text{L}}V_{\text{GPL}}}E_{\text{m}}, \quad E_{\text{T}} = \frac{1 + \xi_{\text{T}}\eta_{\text{T}}V_{\text{GPL}}}{1 - \eta_{\text{T}}V_{\text{GPL}}}E_{\text{m}}. \tag{4}$$

In these relations, η_{L} and η_{T} are expressed as

$$\eta_{\text{L}} = \frac{\dfrac{E_{\text{GPL}}}{E_{\text{m}}} - 1}{\dfrac{E_{\text{GPL}}}{E_{\text{m}}} + \xi_{\text{L}}}, \quad \eta_{\text{T}} = \frac{\dfrac{E_{\text{GPL}}}{E_{\text{m}}} - 1}{\dfrac{E_{\text{GPL}}}{E_{\text{m}}} + \xi_{\text{T}}}, \tag{5}$$

in which E_{m} and E_{GPL} are the elastic moduli of the polymer matrix and GPL, respectively. Also, for ξ_{L} and ξ_{T}, one has

$$\xi_{\text{L}} = 2\left(\frac{a_{\text{GPL}}}{h_{\text{GPL}}}\right), \quad \xi_{\text{T}} = 2\left(\frac{b_{\text{GPL}}}{h_{\text{GPL}}}\right), \tag{6}$$

where a_{GPL}, b_{GPL}, and h_{GPL} stand for the average length, width, and thickness of the GPL, respectively.

Finally, to compute the effective mass density (ρ_{eff}) and effective Poisson's ratio (ν_{eff}) using the corresponding properties of the matrix and GPL, the following relations are used based on the rule of mixture:

$$\rho_{\mathrm{eff}} = \rho_{\mathrm{m}} V_{\mathrm{m}} + \rho_{\mathrm{GPL}} V_{\mathrm{GPL}}, \tag{7a}$$

$$\nu_{\mathrm{eff}} = \nu_{\mathrm{m}} V_{\mathrm{m}} + \nu_{\mathrm{GPL}} V_{\mathrm{GPL}}. \tag{7b}$$

where V_{m} and V_{GPL} denote the volume fractions of the matrix and GPL, respectively.

3 Governing equations

The governing equations are derived based on the classical Donnell shell theory using an energy approach. Moreover, the geometrical nonlinearity is taken into account by the von Kármán hypothesis. The displacement field is written as

$$\begin{cases} u_x(x,y,z) = u(x,y) - z\dfrac{\partial w(x,y)}{\partial x}, \\ u_y(x,y,z) = v(x,y) - z\dfrac{\partial w(x,y)}{\partial y}, \\ u_z(x,y,z) = w(x,y), \end{cases} \tag{8}$$

where $u(x,y)$, $v(x,y)$, and $w(x,y)$ symbolize the middle surface displacements. The nonlinear strain-displacement relations are given by

$$\begin{bmatrix} \varepsilon_{xx} \\ \varepsilon_{yy} \\ \gamma_{xy} \end{bmatrix} = \begin{bmatrix} \varepsilon^0_{xx} \\ \varepsilon^0_{yy} \\ \gamma^0_{xy} \end{bmatrix} - z \begin{bmatrix} \kappa_{xx} \\ \kappa_{yy} \\ \kappa_{xy} \end{bmatrix} = \begin{bmatrix} \dfrac{\partial u}{\partial x} + \dfrac{1}{2}\Big(\dfrac{\partial w}{\partial x}\Big)^2 \\ \dfrac{\partial v}{\partial y} + \dfrac{w}{R} + \dfrac{1}{2}\Big(\dfrac{\partial w}{\partial y}\Big)^2 \\ \dfrac{\partial u}{\partial y} + \dfrac{\partial v}{\partial x} + \dfrac{\partial w}{\partial x}\dfrac{\partial w}{\partial y} \end{bmatrix} - z \begin{bmatrix} \dfrac{\partial^2 w}{\partial x^2} \\ \dfrac{\partial^2 w}{\partial y^2} \\ 2\dfrac{\partial^2 w}{\partial x \partial y} \end{bmatrix}. \tag{9}$$

Furthermore, the stress-strain relations are expressed as

$$\begin{pmatrix} \sigma_{xx} \\ \sigma_{yy} \\ \sigma_{xy} \end{pmatrix}^{(k)} = \begin{pmatrix} Q_{11} & Q_{12} & 0 \\ Q_{12} & Q_{22} & 0 \\ 0 & 0 & Q_{66} \end{pmatrix}^{(k)} \begin{pmatrix} \varepsilon_{xx} \\ \varepsilon_{yy} \\ \gamma_{xy} \end{pmatrix}^{(k)}, \tag{10}$$

where $Q^{(k)}_{11} = Q^{(k)}_{22} = \frac{E_{\mathrm{eff}}}{1-\nu^2_{\mathrm{eff}}}$, $Q^{(k)}_{12} = \frac{\nu_{\mathrm{eff}} E_{\mathrm{eff}}}{1-\nu^2_{\mathrm{eff}}}$, and $Q^{(k)}_{66} = \frac{E_{\mathrm{eff}}}{2(1+\nu_{\mathrm{eff}})}$.

The total strain energy of the shell can be written as

$$\begin{aligned} \Pi_{\mathrm{s}} &= \frac{1}{2}\int_A \int_{-\frac{h}{2}}^{\frac{h}{2}} \sigma_{ij}\varepsilon_{ij}\,\mathrm{d}z\mathrm{d}A = \sum_{l=1}^{N_{\mathrm{L}}} \int_A \int_{z_l}^{z_{l+1}} \sigma^{(l)}_{ij}\varepsilon^{(l)}_{ij}\,\mathrm{d}z\mathrm{d}A \\ &= \frac{1}{2}\int_A \left(N_{xx}\varepsilon^0_{xx} + N_{yy}\varepsilon^0_{yy} + N_{xy}\gamma^0_{xy} + M_{xx}\kappa_{xx} + M_{yy}\kappa_{yy} + M_{xy}\kappa_{xy}\right)\mathrm{d}A, \end{aligned} \tag{11}$$

$$\left(\begin{pmatrix} N_{xx} \\ N_{yy} \\ N_{xy} \end{pmatrix}, \begin{pmatrix} M_{xx} \\ M_{yy} \\ M_{xy} \end{pmatrix}\right) = \sum_{l=1}^{N_{\mathrm{L}}} \int_{z_l}^{z_{l+1}} \begin{pmatrix} \sigma_{xx^{(l)}} \\ \sigma^{(l)}_{yy} \\ \sigma^{(l)}_{xy} \end{pmatrix} (1, z)\,\mathrm{d}z. \tag{12}$$

The resultant forces and moments are formulated as follows:

$$\begin{pmatrix} N_{xx} \\ N_{yy} \\ N_{xy} \\ M_{xx} \\ M_{yy} \\ M_{xy} \end{pmatrix} = \begin{pmatrix} A_{11} & A_{12} & 0 & B_{11} & B_{21} & 0 \\ A_{12} & A_{11} & 0 & B_{21} & B_{11} & 0 \\ 0 & 0 & A_{66} & 0 & 0 & B_{66} \\ B_{11} & B_{21} & 0 & C_{12} & C_{22} & 0 \\ B_{21} & B_{11} & 0 & C_{22} & C_{12} & 0 \\ 0 & 0 & B_{66} & 0 & 0 & C_{66} \end{pmatrix} \begin{pmatrix} \varepsilon_{xx}^0 \\ \varepsilon_{yy}^0 \\ \gamma_{xy}^0 \\ -\dfrac{\partial^2 w}{\partial x^2} \\ -\dfrac{\partial^2 w}{\partial y^2} \\ -2\dfrac{\partial^2 w}{\partial x \partial y} \end{pmatrix}, \quad (13)$$

where

$$(A_{ij}, B_{ij}, C_{ij}) = \sum_{l=1}^{N_{\mathrm{L}}} \int_{z_l}^{z_{l+1}} \left(Q_{ij}^{(k)}, Q_{ij}^{(k)} z, Q_{ij}^{(k)} z^2\right) \mathrm{d}z, \quad i = 1, 2, 6, \quad j = 1, 2, 6.$$

Based on Eq. (9), the following compatibility equation is obtained:

$$\frac{\partial^2 \varepsilon_{xx}^0}{\partial y^2} + \frac{\partial^2 \varepsilon_{yy}^0}{\partial x^2} - \frac{\partial^2 \gamma_{xy}^0}{\partial x \partial y} = \Big(\frac{\partial^2 w}{\partial x \partial y}\Big)^2 - \frac{\partial^2 w}{\partial x^2}\frac{\partial^2 w}{\partial y^2} + \frac{1}{R}\frac{\partial^2 w}{\partial x^2}. \quad (14)$$

Now, one can write

$$N_{xx} = \frac{\partial^2 \varphi}{\partial y^2}, \quad N_{yy} = \frac{\partial^2 \varphi}{\partial x^2}, \quad N_{xy} = -\frac{\partial^2 \varphi}{\partial x \partial y}, \quad (15)$$

in which $\varphi(x, y)$ is the stress function. By inserting Eq. (15) into Eq. (13), one can arrive at

$$\begin{cases} \varepsilon_{xx}^0 = j_0\Big(A_{11}\dfrac{\partial^2 \varphi}{\partial y^2} - A_{12}\dfrac{\partial^2 \varphi}{\partial x^2} + j_1\dfrac{\partial^2 w}{\partial x^2} + j_2\dfrac{\partial^2 w}{\partial y^2}\Big), \\ \varepsilon_{yy}^0 = j_0\Big(A_{11}\dfrac{\partial^2 \varphi}{\partial x^2} - A_{12}\dfrac{\partial^2 \varphi}{\partial y^2} + j_2\dfrac{\partial^2 w}{\partial x^2} + j_1\dfrac{\partial^2 w}{\partial y^2}\Big), \\ \gamma_{xy}^0 = \Big(2B_{66}\dfrac{\partial^2 w}{\partial x \partial y} - \dfrac{\partial^2 \varphi}{\partial x \partial y}\Big)/A_{66}, \end{cases} \quad (16)$$

where $j_0 = \frac{1}{A_{11}^2 - A_{12}^2}$, $j_1 = A_{11}B_{11} - A_{12}B_{12}$, $j_2 = A_{11}B_{12} - A_{12}B_{11}$, and $j_3 = A_{11} - A_{12}$.

Substituting Eq. (16) into Eq. (14) leads to

$$\begin{cases} \nabla^4 \varphi + C_1 \nabla^4 w + C_2\Big(\dfrac{1}{R}\dfrac{\partial^2 w}{\partial x^2} - \Big(\dfrac{\partial^2 w}{\partial x \partial y}\Big)^2 + \dfrac{\partial^2 w}{\partial x^2}\dfrac{\partial^2 w}{\partial y^2}\Big) = 0, \\ C_1 = \dfrac{j_2}{A_{11}}, \quad C_2 = \dfrac{1}{A_{11} j_0}. \end{cases} \quad (17)$$

Now, Eqs. (13) and (16) are inserted into Eq. (11) to obtain the strain energy as

$$\Pi_{\mathrm{s}} = \int_0^{2\pi R} \int_0^L \Big(k_1\Big(\Big(\frac{\partial^2 w}{\partial x^2}\Big)^2 + \Big(\frac{\partial^2 w}{\partial y^2}\Big)^2\Big) + k_2\frac{\partial^2 w}{\partial x^2}\frac{\partial^2 w}{\partial y^2} + k_3\Big(\frac{\partial^2 w}{\partial x \partial y}\Big)^2 + k_4\Big(\Big(\frac{\partial^2 \varphi}{\partial x^2}\Big)^2 + \Big(\frac{\partial^2 \varphi}{\partial y^2}\Big)^2\Big) + k_5\frac{\partial^2 \varphi}{\partial x^2}\frac{\partial^2 \varphi}{\partial y^2} + k_6\Big(\frac{\partial^2 \varphi}{\partial x \partial y}\Big)^2\Big)\mathrm{d}x\mathrm{d}y, \quad (18)$$

where

$$\begin{cases} k_1 = \dfrac{A_{11}\left(B_{11}^2+B_{12}^2\right)-A_{11}^2B_{12}+A_{12}\left(A_{12}B_{12}-2B_{11}B_{12}\right)}{2\left(A_{12}^2-A_{11}^2\right)}, \\ k_2 = \dfrac{A_{12}\left(B_{11}^2+B_{12}^2\right)-A_{12}^2C_{12}+A_{11}\left(A_{11}C_{12}-2B_{11}B_{12}\right)}{A_{11}^2-A_{12}^2}, \\ k_3 = B_{12}-C_{12}+\dfrac{\left(B_{11}-B_{12}\right)^2}{A_{12}-A_{11}}, \quad k_4 = \dfrac{A_{11}}{2\left(A_{11}^2-A_{12}^2\right)}, \\ k_5 = \dfrac{A_{12}}{\left(A_{12}^2-A_{11}^2\right)}, \quad k_6 = \dfrac{1}{\left(A_{11}-A_{12}\right)}. \end{cases} \tag{19}$$

It is considered that the shell is under axial and lateral loads. With Eqs. (9) and (16), the work done by external forces is given by

$$\begin{aligned} \Pi_{\mathrm{ex}} =& q\int_0^{2\pi R}\int_0^L w\mathrm{d}x\mathrm{d}y-\sigma_{0x}h\int_0^{2\pi R}\int_0^L\frac{\partial u}{\partial x}\mathrm{d}x\mathrm{d}y = q\int_0^{2\pi R}\int_0^L w\mathrm{d}x\mathrm{d}y \\ &-\sigma_{0x}h\int_0^{2\pi R}\int_0^L\Big(j_0\Big(A_{11}\frac{\partial^2\varphi}{\partial y^2}-A_{12}\frac{\partial^2\varphi}{\partial x^2}+j_1\frac{\partial^2 w}{\partial x^2}+j_2\frac{\partial^2 w}{\partial y^2}\Big)-\frac{1}{2}\Big(\frac{\partial w}{\partial x}\Big)^2\Big)\mathrm{d}x\mathrm{d}y, \end{aligned} \tag{20}$$

where σ_{0x} denotes the average axial stress, which is positive when the shell is compressed. Also, q stands for the uniform radial pressure.

Now, the total potential energy is obtained as

$$\Pi_{\mathrm{TPE}} = \Pi_{\mathrm{s}} - \Pi_{\mathrm{ex}}. \tag{21}$$

With Eqs. (9) and (16), the circumferential closed condition can be satisfied according to the following relation:

$$\begin{aligned} &\int_0^{2\pi R}\int_0^L\frac{\partial v}{\partial y}\mathrm{d}x\mathrm{d}y \\ &=\int_0^{2\pi R}\int_0^L\Big(j_0\Big(A_{11}\frac{\partial^2\varphi}{\partial x^2}-A_{12}\frac{\partial^2\varphi}{\partial y^2}+j_2\frac{\partial^2 w}{\partial x^2}+j_1\frac{\partial^2 w}{\partial y^2}\Big)+\frac{w}{R}-\frac{1}{2}\Big(\frac{\partial w}{\partial y}\Big)^2\Big)\mathrm{d}x\mathrm{d}y. \end{aligned} \tag{22}$$

The average end-shortening ratio of the cylindrical shell is written as

$$\begin{aligned} \Delta_x =& -\frac{1}{2\pi RL}\int_0^{2\pi R}\frac{\partial u}{\partial x}\mathrm{d}x\mathrm{d}y \\ =& -\frac{1}{2\pi RL}\int_0^{2\pi R}\int_0^L\Big(j_0\Big(A_{11}\frac{\partial^2\varphi}{\partial y^2}-A_{12}\frac{\partial^2\varphi}{\partial x^2}+j_1\frac{\partial^2 w}{\partial x^2}+j_2\frac{\partial^2 w}{\partial y^2}\Big)-\frac{1}{2}\Big(\frac{\partial w}{\partial x}\Big)^2\Big)\mathrm{d}x\mathrm{d}y. \end{aligned} \tag{23}$$

4 Analytical solutions

The deflection of the shell under the combined axial and lateral loading condition can be approximated as[36]

$$w(x,y) = f_0 + f_1\sin(\alpha x)\sin(\beta y) + f_2\left(\sin(\alpha x)\right)^2, \tag{24}$$

in which $\alpha = \frac{m\pi}{L}$ and $\beta = \frac{n}{R}$ (m and n denote the axial half wave number along the x-axis and the wave number along the y-axis, respectively). In addition, f_0, f_1, and f_2 are unknown

amplitudes corresponding to the pre-buckling, linear buckling, and nonlinear buckling states, respectively.

Substitution of Eq. (24) into Eq. (17) leads to

$$\nabla^4\varphi = b_{01}\cos(2\alpha x) + b_{02}\sin(2\beta y) + b_{03}\sin(\alpha x)\sin(\beta y) + b_{04}\sin(3\alpha x)\sin(\beta y)\,, \tag{25}$$

where

$$\begin{aligned}
b_{01} &= \Big(16C_1 f_2\alpha^2 + C_2 f_1\beta^2 - \frac{4C_2 f_2}{R}\Big)\alpha^2/2,\\
b_{02} &= C_2 f_1\alpha^2\beta^2/2,\\
b_{03} &= f_1\Big(C_2\frac{\alpha^2}{R} + C_2 f_2\alpha^2\beta^2 - C_1(\alpha^2+\beta^2)^2\Big),\\
b_{04} &= C_2 f_1 f_2\alpha^2\beta^2.
\end{aligned}$$

Then, the general solution to φ is given by

$$\begin{aligned}
\varphi = {}& b_1\cos(2\alpha x) + b_2\sin(2\beta y) + b_3\sin(\alpha x)\sin(\beta y)\\
&+ b_4\sin(3\alpha x)\sin(\beta y) - \frac{\sigma_{0x}hy^2}{2} - \frac{\sigma_{0y}hx^2}{2},
\end{aligned} \tag{26}$$

where σ_{0y} denotes the average circumferential stress, which is positive for the circumferentially compressed cylindrical shell. Also,

$$\begin{cases}
b_1 = a_1 f_2 + a_2 f_1^2, \quad b_2 = a_3 f_1^2, \quad b_3 = a_4 f_1 f_2 + a_5 f_1, \quad b_4 = a_6 f_1 f_2,\\
a_1 = \dfrac{1}{8}\Big(4C_1 - \dfrac{C_2}{R\alpha^2}\Big), \quad a_2 = \dfrac{C_2\beta^2}{32\alpha^2}, \quad a_3 = \dfrac{C_2\alpha^2}{32\beta^2},\\
a_4 = -\dfrac{C_2\alpha^2\beta^2}{\left(\alpha^2+\beta^2\right)^2}, \quad a_5 = \dfrac{C_2\alpha^2}{R\left(\alpha^2+\beta^2\right)^2} - C_1, \quad a_6 = \dfrac{C_2\alpha^2\beta^2}{\left(9\alpha^2+\beta^2\right)^2}.
\end{cases} \tag{27}$$

By using Eqs. (24) and (26) and defining $k_5 + k_6 = 2k_4$ and $k_2 + k_3 = 2k_1$, Eqs. (18) and (20) are rewritten as

$$\begin{aligned}
\Pi_{\mathrm{s}} = {}& \frac{1}{2}\pi RL\big(k_1 f_1^2\left(\alpha^2+\beta^2\right)^2 + 4\left(2k_1 f_2^2\alpha^4\right)\\
&+ k_4\big(32b_1^2\alpha^4 + 32b_2^2\beta^4 + b_3^2\left(\alpha^2+\beta^2\right)^2 + b_4^2\left(9\alpha^2+\beta^2\right)^2\\
&+ 4h^2\left(k_5\sigma_{0x}\sigma_{0y} + k_4\left(\sigma_{0x}^2 + \sigma_{0y}^2\right)\right)\big)\big),
\end{aligned} \tag{28a}$$

$$\Pi_{\mathrm{ex}} = \pi RL\Big(q\left(2f_0 + f_2\right) + \frac{1}{4}\sigma_{0x}h((f_1^2 + 2f_2^2)\alpha^2 + 8j_0h(A_{11}\sigma_{0x} - A_{12}\sigma_{0y}))\Big). \tag{28b}$$

Using Eqs. (28) and (21) and based on the Ritz method, one can write

$$\frac{\partial\Pi_{\mathrm{TPE}}}{\partial f_0} = \frac{\partial\Pi_{\mathrm{TPE}}}{\partial f_1} = \frac{\partial\Pi_{\mathrm{TPE}}}{\partial f_2} = 0. \tag{29}$$

With Eqs. (24) and (26), Eq. (22) becomes

$$\sigma_{0y} = \frac{1}{A_{11}h}\Big(\frac{2f_0 + f_2}{2j_0R} - \frac{f_1^2\beta^2}{8j_0} + A_{12}\sigma_{0x}h\Big). \tag{30}$$

By inserting Eq. (30) into Eq. (21) and using Eq. (29), one has

$$\begin{aligned}
\frac{\partial\Pi_{\mathrm{TPE}}}{\partial f_0} = {}& \frac{\pi}{2A_{11}^2 j_0^2 R}\big(4k_4\left(2f_0 + f_2\right) + 4A_{11}j_0\left(A_{12}j_0 + k_5\right)\sigma_{0x}h - 4A_{11}^2 j_0^2 qR\\
&- k_4\left(f_1^2\beta^2 - 8A_{12}j_0\sigma_{0x}h\right)\big).
\end{aligned} \tag{31}$$

Considering Eqs. (30) and (31) leads to

$$\sigma_{0y} = \frac{qR}{h}. \tag{32}$$

Considering Eq. (32), using Eq. (29), and noting that $f_1 \neq 0$, one arrives at

$$f_1^2 = -\frac{H_{01} + H_{04} f_2^2 + H_{05} f_2 - \frac{1}{2}\alpha^2 \sigma_{0x} h}{H_{03}}, \tag{33a}$$

$$q = H_{06} f_2 + H_{07} f_1^2 + H_{08} f_1^2 f_2 - \alpha^2 f_2 \sigma_{0x} h, \tag{33b}$$

where

$$\begin{cases} H_{01} = \left(k_1 + k_4 a_5^2\right)\left(\alpha^2+\beta^2\right)^2, \quad H_{03} = 64 k_4 \left(a_2^2\alpha^4 + a_3^2\beta^4\right), \\ H_{04} = k_4\left(a_4^2\left(\alpha^2+\beta^2\right)^2 + a_6^2\left(9\alpha^2+\beta^2\right)^2\right), \quad H_{05} = 2k_4\left(32 a_1 a_2 \alpha^4 + a_4 a_5\left(\alpha^2+\beta^2\right)^2\right), \\ H_{06} = 8\alpha^4\left(k_1 + 4k_4 a_1^2\right), \quad H_{07} = k_4\left(32 a_1 a_2 \alpha^4 + a_4 a_5\left(\alpha^2+\beta^2\right)^2\right), \\ H_{08} = k_4\left(a_4^2\left(\alpha^2+\beta^2\right)^2 + a_6^2\left(9\alpha^2+\beta^2\right)^2\right). \end{cases} \tag{34}$$

From Eqs. (33) and (34), one obtains

$$\sigma_{0x} h = \frac{2\left(H_{01}H_{07} + H_{03}q + \left(H_{01}H_{08} + H_{05}H_{07} - H_{03}H_{06}\right) f_2 + H_{04}H_{08} f_2^3\right)}{\left(H_{07} + \left(H_{08} - 2H_{03}\right) f_2\right)\alpha^2}, \tag{35}$$

which is used to obtain the nonlinear critical condition. Considering $f_2 = 0$, the previous equation is rewritten as follows:

$$\sigma_{0x} h = \frac{2H_{01}}{\alpha^2} + \frac{H_{03} q}{H_{07}\alpha^2}. \tag{36}$$

Equation (36) can be used to derive the interaction relation between axial and lateral linear critical loads, through minimizing σ_{0x} (or q) under a given value of q (or σ_{0x}) for different combinations of m and n. For $q = 0$, one has

$$\begin{aligned} \sigma_{0x} h = & \frac{1}{A_{11}}\left(\frac{A_{11}^2 - A_{12}^2}{R^2}\left(\frac{\alpha}{\alpha^2+\beta^2}\right)^2 + \left(A_{11}C_{11} - B_{11}^2\right)\left(\frac{\alpha}{\alpha^2+\beta^2}\right)^2\right) \\ & + \frac{2\left(A_{12}B_{11} - A_{11}B_{12}\right)}{R}. \end{aligned} \tag{37}$$

By minimizing $\sigma_{0x} h$ with respect to $\left(\frac{\alpha}{\alpha^2+\beta^2}\right)^2$, the linear critical axial compression is obtained as

$$\sigma_{0x\mathrm{cr}} = \frac{2}{A_{11} R h}\left(\sqrt{\left(A_{11}^2 - A_{12}^2\right)\left(A_{11}C_{11} - B_{11}^2\right)} + \left(A_{12}B_{11} - A_{11}B_{12}\right)\right). \tag{38}$$

If $\sigma_{0x} = 0$, the linear critical radial pressure is obtained as

$$\begin{aligned} q = & \frac{2\beta^2}{C_2 R^3\left(\alpha^4+\beta^4\right)\left(\alpha^2+\beta^2\right)^2}\left(C_2\left(9\alpha^4 + 2\alpha^2\beta^2 + \beta^4\right) - 12 C_1 R \alpha^2\left(\alpha^2+\beta^2\right)^2\right) \\ & \cdot\left(C_2^2 k_4 \alpha^4 - 2C_1 C_2 k_4 R \alpha^2\left(\alpha^2+\beta^2\right)^2 + \left(k_1 + C_1^2 k_4\right) R^2\left(\alpha^4+\beta^4\right)\right). \end{aligned} \tag{39}$$

With Eq. (32), Eq. (39) is reduced into the linear critical load of the isotropic shell,

$$\sigma_{0y\mathrm{cr}} = E\left(\frac{\alpha^4}{R^2\beta^2\left(\alpha^2+\beta^2\right)^2} + \frac{h^2\left(\alpha^2+\beta^2\right)^2}{12\beta^2\left(1-\nu_{\mathrm{eff}}^2\right)}\right). \tag{40}$$

Based on Eq. (32), inserting Eqs. (24) and (26) into Eq. (23) results in the following relation for the end-shortening ratio of the shell:

$$\begin{aligned}\Delta_x &= \frac{\alpha^2}{32}(4f_1^2+3f_2^2)+j_0(A_{11}\sigma_{0x}h-A_{12}\sigma_{0y}h)\\ &= \frac{\alpha^2}{32}\Big(3f_2^2-\frac{4}{H_{03}}(H_{01}+H_{04}f_2^2+H_{05}f_2)-\frac{1}{2}\sigma_{0x}\alpha^2h\Big)+j_0(A_{11}\sigma_{0x}h-A_{12}\sigma_{0y}h).\end{aligned}\tag{41}$$

5 Results and discussion

First of all, to check the accuracy of the solution method and presented results, for a special case, the critical buckling load parameters ($\overline{N}^0_{xx}=\sigma_{0x}\times hL^2/(\pi^2D_{\rm m})$; $D_{\rm m}=E_{\rm m}h^3/(12(1-\nu^2))$) of the simply-supported circular cylindrical shell made of FGMs based on the present analysis are compared with those provided by Bagherizadeh et al.[37] in Table 1. The parameters are considered to be $E_{\rm m}=70$ GPa, $E_{\rm c}=380$ GPa, $\nu=\nu_{\rm c}=\nu_{\rm m}=0.3$, $\kappa=2$, and $Z=L^2\sqrt{1-\nu^2}/(Rh)$, where Z is the geometrical parameter. Good agreement can be observed between the results given in Table 1. Furthermore, for a special case, the postbuckling path of the axially-compressed isotropic cylindrical shell is compared with the analytical solution provided by Shen[38], as shown in Fig. 2. Reasonable agreement can be found in the pre-buckling equilibrium response and initial postbuckling path. It is remarked that the difference in the rest of the postbuckling response might be due to mode jump phenomena considered in the present study which were not considered in Ref. [38].

Table 1 Critical buckling load parameters of FGM cylindrical shells under the axial compressive loading

Z	h/R					
	0.01		0.025		0.05	
	Present	Ref. [37]	Present	Ref. [37]	Present	Ref. [37]
50	79.898 5	79.929 6	80.582 5	79.486 84	78.483 6	78.798 42
300	48.022 5	479.506 6	476.033 8	476.383 40	471.771 3	470.877 50
900	1 438.225 4	1 438.157 0	1 431.366 5	1 428.611 00	1 413.647 5	1 412.380 00

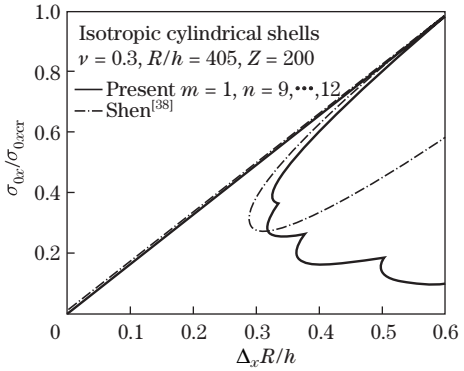

Fig. 2 Comparisons of the postbuckling equilibrium path of axially-compressed isotropic cylindrical shells

To generate numerical results, it is considered that $E_{\rm m}=3$ GPa, $\nu_{\rm m}=0.34$, and $\rho_{\rm m}=2\ 100$ kg/m^3[39]. Moreover, unless otherwise stated, it is assumed that $E_{\rm GPL}=10.1$ TPa, $\nu_{\rm GPL}=0.186$, $\rho_{\rm GPL}=1.062\times10^3$ kg/m^3, $a_{\rm GPL}=2.5$ μm, $b_{\rm GPL}=1.5$ μm, and $h_{\rm GPL}=1.5$ nm[35,40]. Furthermore, unless otherwise stated, $h=0.045$ m and $N_{\rm L}=10$ are considered.

In Tables 2–4, the effects of properties of the GPL on the critical axial stress are studied. In these tables, $\sigma_{\rm cr}$ is tabulated for three distribution patterns of the GPL, i.e., U-GPLRC, X-GPLRC, and O-GPLRC. In Table 2, the results are obtained for various weight fractions of the GPL ranging from 0% to 1.0%. For all distribution patterns, it is clearly observed that the critical axial stress increases with increasing the weight fraction of the GPL. Moreover, it is seen that the critical stress calculated for O-GPLRC is smaller than that for U-GPLRC, and the latter one is also smaller than that for X-GPLRC. Thus, to strength the GPL-RPC shell, GPL fillers should be dispersed near the top and bottom surfaces. In Tables 3 and 4, the effects of length-to-width and length-to-thickness ratios of the GPL on the buckling response of the shell can be studied. One can find that $\sigma_{\rm cr}$ increases as these parameters increase.

Table 2 Critical axial stresses of FG-GPL-RPC cylindrical shells for different distribution patterns and weight fractions of the GPL ($N_{\rm L} = 10$, $R = 40h$, and $L = 2R$)

$w_{\rm GPL}/\%$	$\sigma_{\rm cr}$/MPa		
	U-GPLRC	X-GPLRC	O-GPLRC
0.0	21.58	21.58	21.58
0.1	39.22	44.82	31.99
0.2	56.83	67.59	41.42
0.3	74.41	90.23	50.42
0.5	109.48	135.30	67.76
0.8	161.87	202.59	93.01
1.0	196.65	247.27	109.56

Table 3 Critical axial stresses of FG-GPL-RPC cylindrical shells for different length-to-width ratios of the GPL ($N_{\rm L} = 10$, $R = 40h$, $L = 2R$, $w_{\rm GPL} = 0.3\%$, $b_{\rm GPL} = 1.5$ μm, and $h_{\rm GPL} = 1.5$ nm)

$\frac{a_{\rm GPL}}{b_{\rm GPL}}$	$\sigma_{\rm cr}$/MPa		
	U-GPLRC	X-GPLRC	O-GPLRC
0.5	45.10	52.45	35.21
1.0	58.28	69.48	42.18
1.5	70.44	85.12	48.41
2.0	82.28	100.34	54.36
2.5	93.97	115.37	60.16
3.0	105.60	130.29	65.87

Table 4 Critical axial stresses of FG-GPL-RPC cylindrical shells for different length-to-thickness ratios of the GPL ($N_{\rm L} = 10$, $R = 40h$, $L = 2R$, $w_{\rm GPL} = 0.3\%$, $b_{\rm GPL} = 1.5$ μm, and $a_{\rm GPL} = 2.5$ μm)

$\frac{a_{\rm GPL}}{h_{\rm GPL}}$	$\sigma_{\rm cr}$/MPa		
	U-GPLRC	X-GPLRC	O-GPLRC
500	41.65	47.99	33.34
1 000	51.40	60.60	38.58
1 500	60.12	71.84	43.13
2 000	68.52	82.65	47.44
2 500	76.78	93.27	51.61
3 000	84.96	103.79	55.70

Figure 3 indicates the relation between the nonlinear critical stress and the buckling mode of shells with four patterns considering $w_{\rm GPL} = 0.3\%$. In this figure, for various combinations of mode numbers, σ_{0x} is plotted versus f_2/h. The lowest point of the envelope curve can be regarded as the nonlinear critical axial stress corresponding to the nonlinear buckling mode. Figure 3 reveals that the maximum and minimum values of the critical stress correspond to X-GPLRC and O-GPLRC patterns, respectively.

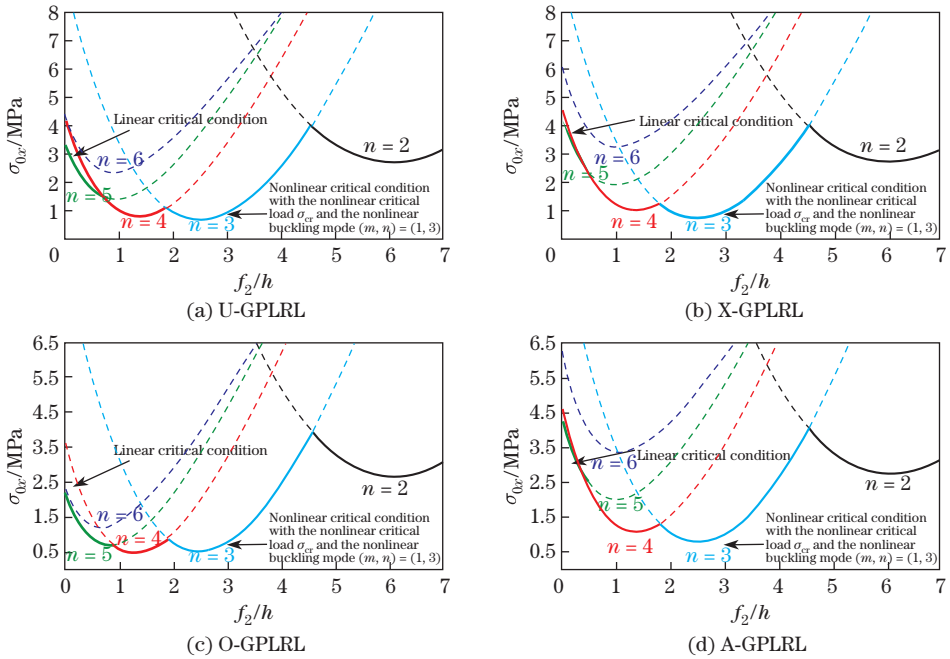

Fig. 3 Diagrammatic sketches of the axial stress and the buckling mode for different distribution patterns of the GPL when $R = 40h$, $L = 2R$, $m = 1$, $n = 2, \cdots, 6$, and $w_{\mathrm{GPL}} = 0.3\%$ (color online)

In Fig. 4, the variation of q for the X-GPLRC shell versus f_2/h is shown for various values of w_{GPL}. The results for pure epoxy are also given in this figure. As expected, with increasing the weight fraction of the GPL, the critical buckling pressure gets larger.

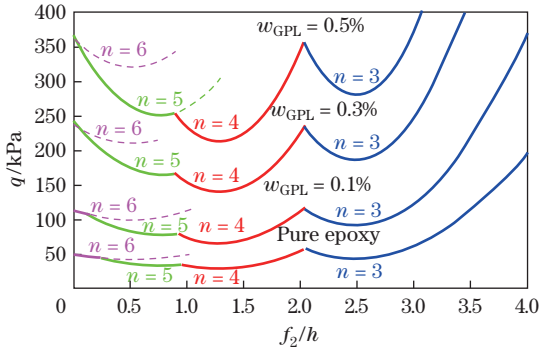

Fig. 4 Relations between the nonlinear critical lateral pressure and the buckling mode for the X-GPLRC shell when $R = 40h$, $L = 2R$, $m = 1$, $n = 3, \cdots, 6$, and $\sigma_{0x} = 0.5$ MPa (color online)

Figure 5 shows the postbuckling paths of X-GPLRC shells. In this figure, solid lines represent the postbuckling path. It is observed that the shell follows a prebuckling path before reaching the linear bifurcation point at which the axial stress takes its maximum value. Thereafter, the shell follows the postbuckling path, and the axial stress considerably decreases to the minimum value which is associated with the lowest critical load. Then, the stress slightly gets larger. The continuous mode jumps are also seen in the postbuckling regions.

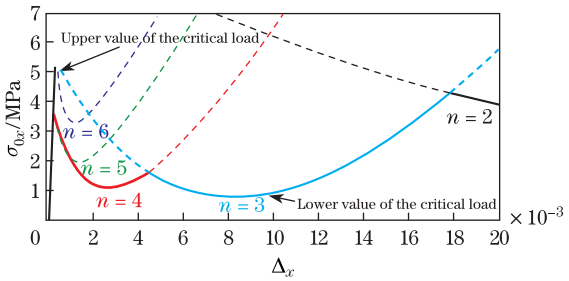

Fig. 5 Postbuckling responses for X-GPLRC shells corresponding to various buckling modes when $R = 40h$, $L = 2R$, $m = 1$, $n = 2, \cdots, 6$, and $w_{\mathrm{GPL}} = 0.3\%$ (color online)

Figure 6 indicates the postbuckling paths of shells with various distribution patterns of the GPL. The results indicate that the postbuckling path of the X-GPLRC shell is above all. The postbuckling path of shells made of pure epoxy is also shown in the figure for the comparison purpose.

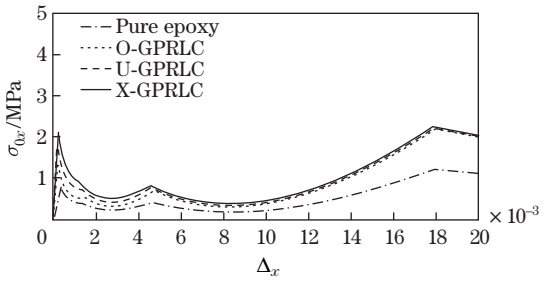

Fig. 6 Postbuckling responses of shells with various distribution patterns of the GPL when $R = 40h$, $L = 2R$, $m = 1$, $n = 2, \cdots, 6$, $w_{\mathrm{GPL}} = 1\%$, and $q = 0$

The effects of the GPL weight fraction, length-to-width ratio, and length-to-thickness ratio on the postbuckling path for X-GPLRC shells are highlighted in Figs. 7–9, respectively. Figure 7 shows that, as the weight fraction of the GPL increases, the critical stress and critical load get larger, and the gradient of linear part of plot increases. From Fig. 8, one can find that the slope of linear part is independent of the length-to-width ratio of the GPL. However, as this ratio goes higher, the critical buckling load increases, and in the postbuckling area, increasing this ratio leads to an increase in the value of the critical postbuckling stress. Furthermore, Fig. 9 indicates that the slope of linear part is independent of the length-to-thickness ratio of the GPL. However, the critical buckling load increases with increasing $a_{\mathrm{GPL}}/h_{\mathrm{GPL}}$. Furthermore, the critical stress increases as this ratio increases in the postbuckling regime.

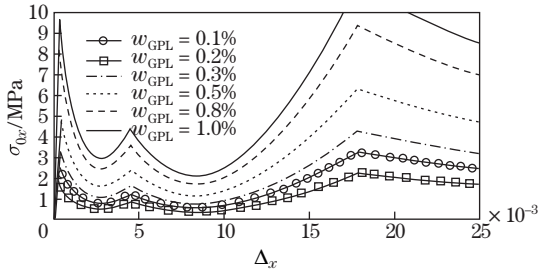

Fig. 7 Effects of the GPL weight fraction on the nonlinear postbuckling response for X-GPLRC shells when $R = 40h$, $L = 2R$, $m = 1$, $n = 2, \cdots, 5$, and $q = 0$ kPa

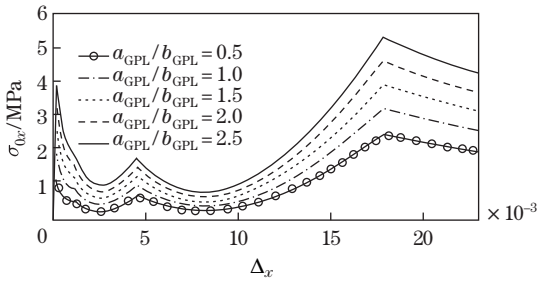

Fig. 8 Effects of the GPL length-to-width ratio on the postbuckling response for X-GPLRC shells when $R = 40h$, $L = 2R$, $m = 1$, $n = 2, \cdots, 5$, and $q = 50$ kPa

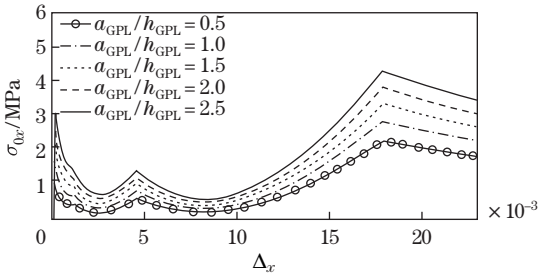

Fig. 9 Effects of the GPL length-to-thickness ratio on the nonlinear postbuckling behavior for X-GPLRC shells when $R = 40h$, $L = 2R$, $m = 1$, $n = 2, \cdots, 5$, and $q = 50$ kPa

Figure 10 shows the postbuckling responses of X-GPLRC shells for various values of the lateral pressure. It is seen that the critical stress decreases as the pressure gets larger.

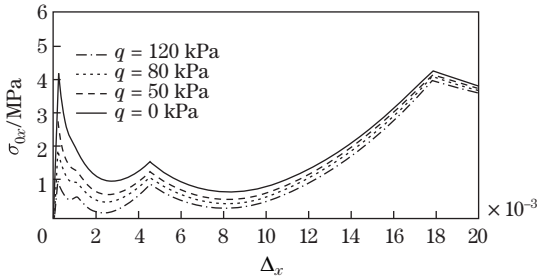

Fig. 10 Postbuckling responses of X-GPLRC shells for various values of the lateral pressure when $R = 40h$, $L = 2R$, $m = 1$, $n = 2, \cdots, 5$, and $w_{GPL} = 0.3\%$

In Fig. 11, the critical axial stresses of shells with various distribution patterns of the GPL are plotted versus the length-to-radius ratio. The mode switching phenomenon can be observed in this figure. It means that, by increasing the length-to-thickness ratio, the critical axial stress may be increased or decreased. Furthermore, it can be seen that, the highest critical axial stress belongs to the X-GPLRC distribution which is followed by U-GPLRC and O-GPLRC distributions and pure epoxy, respectively. Finally, the influence of radius-to-thickness ratio can be investigated in Fig. 12. It is seen that increasing this ratio results in the decrease in the critical stress.

6 Conclusions

In this article, the nonlinear buckling and postbuckling of cylindrical shells reinforced by the GPL under axial compression and lateral pressure are studied by using an analytical approach. The effects of geometrical parameters of the shell, the distribution pattern, geometry, and the weight fraction of the GPL are analyzed. The findings can be summarized as follows.

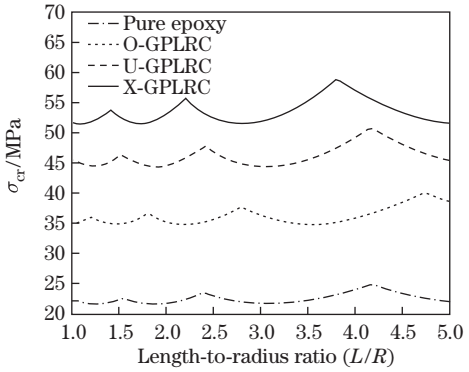

Fig. 11 Variations of critical axial stresses for shells with various distribution patterns of the GPL versus the length-to-radius ratio when $R = 40h$, $m = 1$, $w_{\mathrm{GPL}} = 0.1\%$, and $N_{\mathrm{L}} = 10$

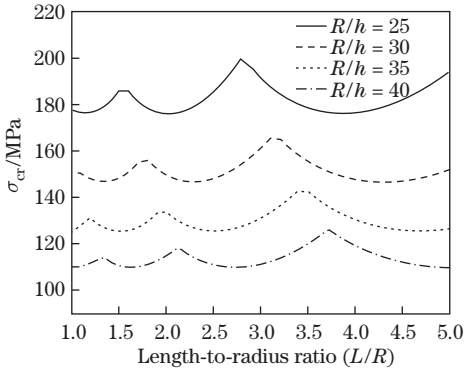

Fig. 12 Variations of critical axial stresses for X-GPLRC shells with various radius-to-thickness ratios versus the length-to-radius ratio when $R = 40h$, $m = 1$, $w_{\mathrm{GPL}} = 0.3\%$, and $N_{\mathrm{L}} = 10$

(i) For all distribution patterns, the critical stress and bucking load increase with increasing the weight fraction of the GPL.

(ii) The distribution pattern X-GPLRC has the largest critical buckling stress and load.

(iii) For small shortening ratios, the difference between the results of various distribution patterns of the GPL is relatively considerable, and for the higher end-shortening ratios, the difference decreases.

(iv) The length-to-width and length-to-thickness ratios of the GPL do not affect the linear part of the load-shortening ratio response curve. On the other hand, increasing these ratios leads to the increase of the critical buckling load in the shell buckling zone and the critical stress of postbuckling.

References

[1] ZHU, Y., DAI, Y., MA, Q., and TANG, W. Buckling of externally pressurized cylindrical shell: a comparison of theoretical and experimental data. *Thin-Walled Structures*, **129**, 309–316 (2018)

[2] LI, Z. M., LIU, T., and YANG, D. Q. Postbuckling behavior of shear deformable anisotropic laminated cylindrical shell under combined external pressure and axial compression. *Composite Structures*, **198**, 84–108 (2018)

[3] LI, Z. M. and QIAO, P. Buckling and postbuckling of anisotropic laminated cylindrical shells under combined external pressure and axial compression in thermal environments. *Composite Structures*, **119**, 709–726 (2015)

[4] HUANG, H. and HAN, Q. Nonlinear buckling and postbuckling of heated functionally graded cylindrical shells under combined axial compression and radial pressure. *International Journal of Non-Linear Mechanics*, **44**(2), 209–218 (2009)

[5] SHAKOURI, M., SHARGHI, H., and KOUCHAKZADEH, M. Torsional buckling of generally laminated conical shell. *Meccanica*, **52**(4/5), 1051–1061 (2017)

[6] SOFIYEV, A. Application of the FOSDT to the solution of buckling problem of FGM sandwich conical shells under hydrostatic pressure. *Composites Part B*: *Engineering*, **144**, 88–98 (2018)

[7] GUO, J., CHEN, J., and PAN, E. Analytical three-dimensional solutions of anisotropic multilayered composite plates with modified couple-stress effect. *Composite Structures*, **153**, 321–331 (2016)

[8] GUO, J., CHEN, J., and PAN, E. Size-dependent behavior of functionally graded anisotropic composite plates. *International Journal of Engineering Science*, **106**, 110–124 (2016)

[9] SHOKRIEH, M. and RAFIEE, R. A review of the mechanical properties of isolated carbon nanotubes and carbon nanotube composites. *Mechanics of Composite Materials*, **46**(2), 155–172 (2010)

[10] ASHRAFI, B., HUBERT, P., and VENGALLATORE, S. Carbon nanotube-reinforced composites as structural materials for microactuators in microelectromechanical systems. *Nanotechnology*, **17**(19), 4895–4903 (2006)

[11] ESAWI, A. M. and FARAG, M. M. Carbon nanotube reinforced composites: potential and current challenges. *Materials and Design*, **28**(9), 2394–2401 (2007)

[12] TJONG, S. C. *Carbon Nanotube Reinforced Composites*: *Metal and Ceramic Matrices*, John Wiley & Sons, Weinheim (2009)

[13] BAKSHI, S., LAHIRI, D., and AGARWAL, A. Carbon nanotube reinforced metal matrix composites: a review. *International Materials Reviews*, **55**(1), 41–64 (2010)

[14] EBRAHIMI, F. and FARAZMANDNIA, N. Thermo-mechanical vibration analysis of sandwich beams with functionally graded carbon nanotube-reinforced composite face sheets based on a higher-order shear deformation beam theory. *Mechanics of Advanced Materials and Structures*, **24**(10), 820–829 (2017)

[15] FU, Y., ZHONG, J., SHAO, X., and TAO, C. Analysis of nonlinear dynamic stability for carbon nanotube-reinforced composite plates resting on elastic foundations. *Mechanics of Advanced Materials and Structures*, **23**(11), 1284–1289 (2016)

[16] THOSTENSON, E. T., REN, Z., and CHOU, T. W. Advances in the science and technology of carbon nanotubes and their composites: a review. *Composites Science and Technology*, **61**(13), 1899–1912 (2001)

[17] LAU, K. T., GU, C., GAO, G. H., LING, H. Y., and REID, S. R. Stretching process of single- and multi-walled carbon nanotubes for nanocomposite applications. *Carbon*, **42**(2), 426–428 (2004)

[18] VEEDU, V. P., CAO, A., LI, X., MA, K., SOLDANO, C., KAR, S., AJAYAN, P. M., and GHASEMI-NEJHAD, M. N. Multifunctional composites using reinforced laminae with carbon-nanotube forests. *Nature Materials*, **5**(6), 457–462 (2006)

[19] KIM, M., PARK, Y. B., OKOLI, O. I., and ZHANG, C. Processing, characterization, and modeling of carbon nanotube-reinforced multiscale composites. *Composites Science and Technology*, **69**(3), 335–342 (2009)

[20] SUN, K., YU, J., ZHANG, C., and ZHOU, X. In situ growth carbon nanotube reinforced SiC_f/SiC composite. *Materials Letters*, **66**(1), 92–95 (2012)

[21] AHMADI, M., ANSARI, R., and HASSANZADEH-AGHDAM, M. Low velocity impact analysis of beams made of short carbon fiber/carbon nanotube-polymer composite: a hierarchical finite element approach. *Mechanics of Advanced Materials and Structures* (2018) https://doi.org/10.1080/15376494.2018.1430276

[22] JI, X. Y., CAO, Y. P., and FENG, X. Q. Micromechanics prediction of the effective elastic moduli of graphene sheet-reinforced polymer nanocomposites. *Modelling and Simulation in Materials Science and Engineering*, **18**(4), 045005 (2010)

[23] TERRONES, M. and TERRONES, H. The carbon nanocosmos: novel materials for the twenty-first century. *Philosophical Transactions of the Royal Society of London A*: *Mathematical*, *Physical and Engineering Sciences*, **361**(1813), 2789–2806 (2003)

[24] SHI, G., ARABY, S., GIBSON, C. T., MENG, Q., ZHU, S., and MA, J. Graphene platelets and their polymer composites: fabrication, structure, properties, and applications. *Advanced Functional Materials*, **28**(19), 1706705 (2018)

[25] GHOLAMI, R. and ANSARI, R. Nonlinear harmonically excited vibration of third-order shear deformable functionally graded graphene platelet-reinforced composite rectangular plates. *Engineering Structures*, **156**, 197–209 (2018)

[26] RAFIEE, M., NITZSCHE, F., and LABROSSE, M. Modeling and mechanical analysis of multiscale fiber-reinforced graphene composites: nonlinear bending, thermal post-buckling and large amplitude vibration. *International Journal of Non-Linear Mechanics*, **103**, 104–112 (2018)

[27] LIU, D., KITIPORNCHAI, S., CHEN, W., and YANG, J. Three-dimensional buckling and free vibration analyses of initially stressed functionally graded graphene reinforced composite cylindrical shell. *Composite Structures*, **189**, 560–569 (2018)

[28] GHOLAMI, R. and ANSARI, R. On the nonlinear vibrations of polymer nanocomposite rectangular plates reinforced by graphene nanoplatelets: a unified higher-order shear deformable model. *Iranian Journal of Science and Technology*, *Transactions of Mechanical Engineering* (2018) https://doi.org/10.1007/s40997-018-0182-9

[29] KITIPORNCHAI, S., CHEN, D., and YANG, J. Free vibration and elastic buckling of functionally graded porous beams reinforced by graphene platelets. *Materials and Design*, **116**, 656–665 (2017)

[30] SONG, M., YANG, J., and KITIPORNCHAI, S. Bending and buckling analyses of functionally graded polymer composite plates reinforced with graphene nanoplatelets. *Composites Part B*: *Engineering*, **134**, 106–113 (2018)

[31] GHOLAMI, R. and ANSARI, R. Large deflection geometrically nonlinear analysis of functionally graded multilayer graphene platelet-reinforced polymer composite rectangular plates. *Composite Structures*, **180**, 760–771 (2017)

[32] WANG, Y., FENG, C., ZHAO, Z., and YANG, J. Buckling of graphene platelet reinforced composite cylindrical shell with cutout. *International Journal of Structural Stability and Dynamics*, **18**(3), 1850040 (2018)

[33] WANG, Y., FENG, C., ZHAO, Z., LU, F., and YANG, J. Torsional buckling of graphene platelets (GPLs) reinforced functionally graded cylindrical shell with cutout. *Composite Structures*, **197**, 72–79 (2018)

[34] YANG, J., WU, H., and KITIPORNCHAI, S. Buckling and postbuckling of functionally graded multilayer graphene platelet-reinforced composite beams. *Composite Structures*, **161**, 111–118 (2017)

[35] RAFIEE, M. A., RAFIEE, J., WANG, Z., SONG, H., YU, Z. Z., and KORATKAR, N. Enhanced mechanical properties of nanocomposites at low graphene content. *ACS Nano*, **3**(12), 3884–3890 (2009)

[36] VOL'MIR, A. D. S. *Stability of Elastic Systems*, Foreign Technology Division, Wright-Patterson Air Force Base, Ohio (1965)

[37] BAGHERIZADEH, E., KIANI, Y., and ESLAMI, M. Mechanical buckling of functionally graded material cylindrical shells surrounded by Pasternak elastic foundation. *Composite Structures*, **93**(11), 3063–3071 (2011)

[38] SHEN, H. S. Postbuckling analysis of axially-loaded functionally graded cylindrical shells in thermal environments. *Composites Science and Technology*, **62**(7/8), 977–987 (2002)

[39] YASMIN, A. and DANIEL, I. M. Mechanical and thermal properties of graphite platelet/epoxy composites. *Polymer*, **45**(24), 8211–8219 (2004)

[40] LIU, F., MING, P., and LI, J. Ab initio calculation of ideal strength and phonon instability of graphene under tension. *Physical Review B*, **76**(6), 064120 (2007)